A Nonlinear Sparse Representation-Based Binary Hypothesis Model for Hyperspectral Target Detection

Yuxiang Zhang, *Student Member, IEEE*, Liangpei Zhang, *Senior Member, IEEE*, Bo Du, *Member, IEEE*, and Shugen Wang, *Member, IEEE*

***Abstract*—The sparsity model has been employed for hyperspectral target detection and has been proved to be very effective when compared to the traditional linear mixture model. However, the state-of-art sparsity models usually represent a test sample via a sparse linear combination of both target and background training samples, which does not result in an efficient representation of a background test sample. In this paper, a sparse representation-based binary hypothesis (SRBBH) model employs more appropriate dictionaries with the binary hypothesis model to sparsely represent the test sample. Furthermore, the nonlinear issue is addressed in this paper, and a kernel method is employed to resolve the detection issue in complicated hyperspectral images. In this way, the kernel SRBBH model not only takes the nonlinear endmember mixture into consideration, but also fully exploits the sparsity model by the use of more reasonable dictionaries. The recovery process leads to a competition between the background and target subspaces, which is effective in separating the targets from the background, thereby enhancing the detection performance.**

***Index Terms*—Binary hypothesis, hyperspectral imagery (HSI), kernel, sparse representation, target detection.**

I. Introduction

HYPERSPECTRAL remote sensing has attracted a booming interest in recent years, as hyperspectral imaging sensors have broadband wavelength and a very fine spectral resolution, which can provide abundant material information [1], [2]. The ample spectral information available in hyperspectral data can be used to achieve a variety of tasks that cannot be undertaken with the spatial information-based methods. Hyperspectral imagery (HSI) data have been widely used in civil and military applications, such as rare mineral exploration, agricultural yield estimation, landmine detection, and battleground reconnaissance and surveillance applications [3]–[6].

Manuscript received May 13, 2014; revised October 15, 2014; accepted October 30, 2014. Date of publication November 25, 2014; date of current version July 30, 2015. This work was supported in part by the National Basic Research Program of China (973 Program) under Grant 2011CB707105 and Grant 2012CB719905, the National Natural Science Foundation of China under Grant 41431175 and Grant 61471274.

Y. Zhang and S. Wang are with the School of Remote Sensing and Information Engineering, Wuhan University, Wuhan 430079, China (e-mail: zyx_070504@163.com; wangsg@whu.edu.cn).

B. Du is with the School of Computer, Wuhan University, Wuhan 430079, China (e-mail: gunspace@163.com).

L. Zhang is with the State Key Laboratory of Information Engineering in Surveying, Mapping, and Remote Sensing, Wuhan University, Wuhan 430079, China (e-mail: zlp62@whu.edu.cn).

Color versions of one or more of the figures in this paper are available online at http://ieeexplore.ieee.org.

Digital Object Identifier 10.1109/JSTARS.2014.2368173

Target detection is one of the most important applications of HSI, where pixels are labeled as target or background, and the targets of interest are separated from the background mainly based on the spectral information. The main difficulties of target detection lie in spectral variation and subpixel target detection. Subpixel spectral detection arises as a result of the limitation of the spatial resolution of HSI, which brings about the fact that one pixel usually contains several different kinds of materials [3], [7]. As a result, the signal of a mixed pixel is a combination of these corresponding materials' spectra. The linear mixture model (LMM), which models a pixel as a linear mixture of endmembers in the image scene, has shown great success in subpixel detection for HSI [8]. Accordingly, a number of LMM-based target detection algorithms have been developed, such as the adaptive coherence estimator (ACE) [9] and the matched subspace detector (MSD) [10]. These algorithms estimate the abundance of targets contained in an image pixel to decide whether the pixel is a target or not. However, this abundance information may be inaccurate, due to the fact that it is easily affected by noise [11], and the limited endmembers usually lead to a poor representation of a large number of pixels with similar spectral characteristics.

In recent years, sparse representation has been proposed and has been proved to be a powerful approach in sparsely representing pixels' spectra by the use of only a few training samples in the image [12]. To strengthen the performance of the LMM, sparsity representation-based detection methods have been developed, including the sparsity-based target detector (STD) [13], the joint sparse detector (JSD) [14], and the algorithm in [15]. These detection methods linearly model a test sample as a linear mixture of a number of training samples from target and background dictionaries. Furthermore, the background dictionary is usually a local one consisting of the neighboring pixels, which are similar materials with highly correlated spectral characteristics. Therefore, the sparsity model in these detectors, which can be regarded as a generalized LMM (GLMM), often obtains a good representation of the test pixel. However, this sparsity model represents not only the target pixels, but also the background pixels, with both target and background training samples, which may lead to a poor representation of a background pixel, and result in a final weakened detection performance. The sparse representation-based binary hypothesis (SRBBH) model is proposed to solve this problem. The SRBBH model linearly models the background pixels with background training samples under the null hypothesis, and the

target pixels with both target and background training samples under the alternative hypothesis. In others words, a background pixel is sparsely represented by background-only training samples, and a target pixel, which is likely to be a mixed pixel, is sparsely represented via both target and background training samples.

However, when electromagnetic waves reflect off surfaces that are composed of an intimate mixture of various material components, or the surfaces are not flat, multiple bounces are common, and the spectral mixing may become nonlinear [16]. In such cases, the LMMs, including the GLMM-based detectors, are not flexible enough to fully exploit the complex data structure [17]. The detector based on the sparse representation-based binary hypothesis model for detection (SRBBHD) may not exploit the nonlinear correlation between the spectral bands in real HSI, which makes it inadequate for some nonlinearly mixed scenes. However, the traditional LMM can be easily extended to a nonlinear version, and a lot of kernel-based detectors have been developed, such as the kernel-matched subspace detector (KMSD) [2], kernel-constrained energy minimization (KCEM) [18], the kernel spectral-matched filter (KSMF) [19], and the kernel-based target-constrained interference-minimized filter (KTCIMF) [16]. As with these state-of-art kernel algorithms, SRBBHD can be developed into a kernelized version, which is labeled here as KSRBBHD. Taking both the spectral signal representation and the complex data structure in a real HSI scene into consideration, KSRBBHD is intended to separately represent the target and background in a high-dimensional feature space, so as to obtain a better detection performance.

The rest of the paper is organized as follows. Section II briefly reviews the basic STD and kernel methods and kernel tricks. Section III proposes the KSRBBHD method for HSI. The effectiveness of the proposed model and the detection algorithm is demonstrated by extensive experiments presented in Section IV. Finally, conclusion is drawn in Section V.

II. Brief Review of Related Works

A. STD

In the sparsity model in STD [13], it is assumed that a test sample $\mathbf{x}$ can be approximated by a sparse linear combination of elements from all the classes (target and background). A hyperspectral signal can be denoted as $\mathbf{x} \in \mathbb{R}^B$, where B is the number of bands. Given a matrix $\mathbf{A} \in \mathbb{R}^{\mathrm{B}\times\mathrm{N}}$ with $N \gg B$ as an overcomplete dictionary, which is constructed by the background training samples $\{\mathbf{a}_i^b\}_{i=1,2,\ldots N_b}$ and the target training samples $\{\mathbf{a}_i^t\}_{i=1,2,\ldots N_t}$, it is believed that the signal can be approximately represented by multiplying the dictionary with a sparse vector, as follows [13]:

$$\begin{aligned}\mathbf{x} &\approx \left(\alpha_1^b\mathbf{a}_1^b + \cdots + \alpha_{N_b}^b\mathbf{a}_{N_b}^b\right) + \left(\alpha_1^t\mathbf{a}_1^t + \cdots + \alpha_{N_t}^t\mathbf{a}_{N_t}^t\right)\\ &= \left[\,\mathbf{a}_1^b\ \mathbf{a}_2^b\ \cdots\ \mathbf{a}_{N_b}^b\,\right]\left[\,\alpha_1^b\ \alpha_2^b\ \cdots\ \alpha_{N_b}^b\,\right]^T\\ &\quad + \left[\,\mathbf{a}_1^t\ \mathbf{a}_2^t\ \cdots\ \mathbf{a}_{N_t}^t\,\right]\left[\,\alpha_1^t\ \alpha_2^t\ \cdots\ \alpha_{N_t}^t\,\right]^T\\ &= \mathbf{A}^b\boldsymbol{\alpha}^b + \boldsymbol{A}^t\boldsymbol{\alpha}^t = \mathbf{A}\boldsymbol{\alpha}\end{aligned} \tag{1}$$

where N_b and N_t are the number of background and target training samples, respectively. $\mathbf{A}^b$ and $\mathbf{A}^t$ are the $B \times N_b$ background dictionary and $B \times N_t$ target dictionary, whose columns are the background and target training samples, respectively. $\mathbf{A}$ is the union dictionary consisting of both the background and target training samples. $\boldsymbol{\alpha}$ is a concatenation of $\boldsymbol{\alpha}^b$ and $\boldsymbol{\alpha}^t$, which are sparse vectors with only a few nonzero entries.

The sparse vector $\boldsymbol{\alpha}$ can be recovered by solving

$$\widehat{\boldsymbol{\alpha}} = \arg\min \|\mathbf{A}\boldsymbol{\alpha} - \mathbf{x}\|_2 \quad \text{subject to} \quad \|\boldsymbol{\alpha}\|_0 \le K_0 \tag{2}$$

where $\|\cdot\|_0$ denotes the ℓ_0-norm, which is defined as the number of nonzero entries in the vector (also called the sparsity level of the vector) [13]. K_0 is a given upper bound on the sparsity level [20]. In this paper, the above problem is solved by the orthogonal matching pursuit (OMP) [21] algorithm.

Partially, reconstructed pixels, using only the background or target dictionary, can be obtained by decomposing the sparse vector $\widehat{\boldsymbol{\alpha}}$ into $\widehat{\boldsymbol{\alpha}}^b$ and $\widehat{\boldsymbol{\alpha}}^t$, which are the vectors, respectively, corresponding to the background and target training samples. The recovery process implicitly leads to a competition between the background and target subspaces. The residuals of recovery by the background and target subspaces are [13]

$$\begin{aligned} r_b(\mathbf{x}) &= \left\|\mathbf{x} - \mathbf{A}^b\widehat{\boldsymbol{\alpha}}^b\right\| \\ r_t(\mathbf{x}) &= \left\|\mathbf{x} - \mathbf{A}^t\widehat{\boldsymbol{\alpha}}^t\right\|. \end{aligned} \tag{3}$$

The class label of the test pixel can be determined by these residuals, and the output of the detector is calculated by [13]

$$D_{\mathrm{STD}}(\mathbf{x}) = r_b(\mathbf{x}) - r_t(\mathbf{x}). \tag{4}$$

B. Kernel Methods and the Kernel Trick

Kernel methods have attracted great interest over the past decades and have shown their superiority in nonlinear feature extraction and classification [22], [23]. The idea is to use a nonlinear function Φ which can map the original linearly inseparable data to a high-dimensional space where the data are assumed to be linearly separable.

Suppose that the input hyperspectral data are represented by the data space $\boldsymbol{\chi}$, and $\boldsymbol{\chi}$ is mapped into feature space $\mathbf{F}$ via function Φ

$$\begin{aligned} \Phi &: \boldsymbol{\chi} \to \mathbf{F} \\ \mathbf{x} &\to \Phi(\mathbf{x}) \end{aligned} \tag{5}$$

where $\mathbf{x}$ is an input vector in $\boldsymbol{\chi}$. Due to the high dimensionality, it is not computationally feasible to directly implement an algorithm in this feature space. However, kernel-based learning algorithms use an effective kernel trick to implement dot products in the feature space in terms of kernel functions [24], without knowing the exact mapping function Φ.

The kernel representation for the dot products is expressed as

$$\mathbf{K}_{ij} = \mathbf{K}(\mathbf{x}_i, \mathbf{x}_j) = <\Phi(\mathbf{x}_i), \Phi(\mathbf{x}_j)> = \Phi(\mathbf{x}_i)\cdot\Phi(\mathbf{x}_j). \tag{6}$$

There are three commonly used kernel functions: the Gaussian radial basis function (RBF)s, the polynomial kernel,

and the sigmoid kernel. Among them, the Gaussian RBF kernel is more widely adopted. It is given by

$$\mathbf{K}(\mathbf{x},\mathbf{y}) = \exp\left(-\frac{\|\mathbf{x}-\mathbf{y}\|^2}{2\sigma^2}\right) \tag{7}$$

where σ is an important kernel parameter, and $2\sigma^2$ represents the width of the Gaussian RBF kernel [25]. In this study, the value of σ was determined experimentally. In our future work, we will investigate how to automatically choose the appropriate values of σ for different hyperspectral images. Detailed information about the properties of different kernels and kernel-based learning can be found in [24].

III. SRBBHD Method and the Kernelized Version

In this section, we introduce the proposed sparsity-based target detection algorithm for HSI, which utilizes the full class information of the training samples to construct more reasonable dictionaries, and a kernelized version of the detector to better separate the complicated background and target. We first introduce the novel sparsity-based model.

A. SRBBHD

The sparsity model in (1) may not be suitable for background pixels. The reason for this is that a background pixel does not, theoretically, contain the target spectrum, and the target sparse vector is ideally a zero vector, but this may not always be the case. Even if the background and target training samples have distinct spectral signatures and lie in different subspaces, the background and target subspaces are usually not orthogonal, due to the spectral variation. Furthermore, the background sparse vector is simultaneously recovered with the target sparse vector in the sparsity model; therefore, the two sparse vectors are likely to affect each other, which finally leads to a nonzero target sparse vector. The SRBBHD solves this problem by utilizing a binary hypothesis model with more reasonable dictionaries, where the test pixel can be modeled with background training samples under the null hypothesis, and with target and background training samples under the alternative hypothesis.

In detail, if $\mathbf{x}$ is a background pixel, it belongs to the H_0 hypothesis, and the spectrum approximately lies in a low-dimensional subspace spanned by the background training samples $\{\mathbf{a}_i^b\}_{i=1,2,\ldots N_b}$ from background dictionary $\mathbf{A}^b$. On the other hand, if $\mathbf{x}$ is a target pixel belonging to the H_1 hypothesis, the observed spectrum approximately lies in the union of the background and target subspaces spanned by both the background training samples $\{\mathbf{a}_i^b\}_{i=1,2,\ldots,N_b}$ and the target training samples $\{\mathbf{a}_i^t\}_{i=1,2,\ldots,N_t}$ from the union dictionary $\mathbf{A}$. Therefore, a test sample pixel can be modeled by

$$\begin{aligned} H_0 &: \mathbf{x} \approx \mathbf{A}^b\boldsymbol{\gamma}, \quad \text{target absent} \\ H_1 &: \mathbf{x} \approx \mathbf{A}^b\boldsymbol{\beta}^b + \mathbf{A}^t\boldsymbol{\beta}^t = \mathbf{A}\boldsymbol{\beta} \quad \text{target present} \end{aligned} \tag{8}$$

where $\boldsymbol{\gamma}$ and $\boldsymbol{\beta}$ are vectors whose entries, respectively, correspond to the weighting of the samples in $\mathbf{A}^b$ and $\mathbf{A}$. With the sparsity employed for both hypotheses, the residuals under the two hypotheses are comparable. We can see that both STD and SRBBHD originate from sparse representation theory in the classification field. The difference between them is that SRBBHD further utilizes the class label information of the training samples and models the test pixel using different training samples, according to the assumed class label of the test pixel, while STD models the test pixel without considering the assumed class label of the test pixel. In other words, the two competing hypotheses in STD are both derived from the same reconstruction process, whereas SRBBHD further digs into the internal structure of a test pixel by two different reconstruction processes.

The construction of dictionaries $\mathbf{A}^b$ and $\mathbf{A}$ requires careful attention. In this paper, an adaptive local dictionary method [13] is employed to construct the background dictionary, in order to better represent and capture the spectral signature of the test sample. As the number of target pixels is small, the target dictionary is, therefore, constructed by some of the target pixels in the global image scene. Specifically, the background dictionary is generated locally for each test pixel through a dual concentric window [26]. Since there is no specific method for choosing the size of the detection window [27], the window sizes are set manually and experientially. Only pixels in the outer region form the atoms in $\mathbf{A}^b$.

The sparse vectors $\boldsymbol{\gamma}$ and $\boldsymbol{\beta}$ can be recovered by solving:

$$\begin{aligned} \widehat{\boldsymbol{\gamma}} &= \arg\min \|\mathbf{A}^b\boldsymbol{\gamma} - \mathbf{x}\|_2 \quad \text{subject to} \quad \|\boldsymbol{\gamma}\|_0 \le K_0 \\ \widehat{\boldsymbol{\beta}} &= \arg\min \|\mathbf{A}\boldsymbol{\beta} - \mathbf{x}\|_2 \quad \text{subject to} \quad \|\boldsymbol{\beta}\|_0 \le K_0 \end{aligned} \tag{9}$$

where $\widehat{\boldsymbol{\gamma}}$ and $\widehat{\boldsymbol{\beta}}$ are the recovered sparse vectors, which are recovered by, respectively, decomposing the test pixel over the given dictionaries $\mathbf{A}^b$ and $\mathbf{A}$ to find the few atoms that best represent the test pixel under the different hypotheses.

As for the computational complexity, since SRBBHD solves two STD-like optimization problems, the time cost of SRBBHD is about twice that of STD at the same sparsity level.

Whether the same sparsity levels should be used in both hypotheses during the recovery process is an interesting problem. If the sparsity levels are set differently in both hypotheses, and especially if the sparsity level in H_1 is higher than that in the null hypothesis, from a reconstruction point of view, the target and background subspaces will, therefore, have a higher dimension with a richer basis, and consequently they will always represent the test pixel (background or target) more accurately. Thus, theoretically, the H_1 residual should always be smaller than the H_0 residual. Hence, the same sparsity levels should be used in both hypotheses, which can greatly help to reduce the complexity of the parameter adjustment. As we know, the recovery process aims to find a certain number of atoms from $\mathbf{A}^b$ or $\mathbf{A}$ that best represent the test pixel. Therefore, when the same sparsity levels are set for both hypotheses, for a background test pixel, the reconstruction residuals of the two hypotheses tend to be the same. For a target pixel, the reconstruction residual via target and background samples in $\mathbf{A}$ tends to be smaller than that through the same number of only background samples in $\mathbf{A}^b$. Therefore,

based on the same sparsity level constraint, the recovery process implicitly leads to a competition between the two hypotheses. The residuals of recovery by the two hypotheses are

$$\begin{aligned} r_0(\mathbf{x}) &= \left\|\mathbf{x} - \mathbf{A}^b\widehat{\boldsymbol{\gamma}}\right\| \\ r_1(\mathbf{x}) &= \left\|\mathbf{x} - \mathbf{A}\widehat{\boldsymbol{\beta}}\right\|. \end{aligned} \tag{10}$$

The class label of the test pixel can be determined by these residuals. In addition, the output of the detector is calculated by

$$D_{\mathrm{SRBBHD}}(\mathbf{x}) = r_0(\mathbf{x}) - r_1(\mathbf{x}). \tag{11}$$

B. Kernelization of SRBBHD

For a hyperspectral scene, a pixel spectrum is usually composed of a mixture of various material components. In addition, when electromagnetic waves reflect off the surfaces, the surfaces are usually not flat, and multiple bounces are common. Therefore, based on this complex imaging environment and conditions, the data structure can be very complex, and the spectral mixing may become nonlinear [16]. In such cases, the linear SRBBHD may be not flexible enough to fully exploit the complex data structure. It is therefore necessary to transform the linear SRBBH model into a nonlinear version and develop a kernelized SRBBHD (KSRBBHD) by mapping the input data into a potentially infinite dimensional feature space by a suitable kernel method, and the nonlinear version is transformed into a linear version in the feature space [22]–[24].

We suppose that the vector $\Phi(\mathbf{x})$ in the feature space can be represented by a sparse linear combination of the training samples $\{\mathbf{d}_i^b\}_{i=1,2,\ldots N_d}$, which can be expressed as [28]

$$\Phi(\mathbf{x}) \approx \left[\begin{array}{ccc}\Phi(\mathbf{d}_1) & \cdots & \Phi(\mathbf{d}_{N_d})\end{array}\right]\left[\begin{array}{ccc}\omega_1 & \cdots & \omega_{N_d}\end{array}\right]^T = \mathbf{D}_\Phi\boldsymbol{\omega} \tag{12}$$

where $\mathbf{D}_\Phi$ is the training dictionary in the feature space, and $\boldsymbol{\omega}$ is a sparse vector. The vector ω can be recovered by solving [28]

$$\widehat{\boldsymbol{\omega}} = \arg\min \|\mathbf{D}_\Phi\boldsymbol{\omega} - \Phi(\mathbf{x})\|_2 \quad \text{subject to } \|\boldsymbol{\omega}\|_0 \le K_0. \tag{13}$$

The above problem can be approximately solved by kernelized sparse recovery algorithms, such as kernelized orthogonal matching pursuit (KOMP) [29]. The residual between the test sample and the reconstruction is then computed by

$$r(\mathbf{x}) = \|\Phi(\mathbf{x}) - \mathbf{D}_\Phi\widehat{\boldsymbol{\omega}}\|. \tag{14}$$

Employing the RBF kernel function, the residual can be expressed as [28]

$$\begin{aligned} r(\mathbf{x}) &= \|\Phi(\mathbf{x}) - \mathbf{D}_\Phi\widehat{\boldsymbol{\omega}}\| \\ &= \left(k(\mathbf{x},\mathbf{x}) - 2\widehat{\boldsymbol{\omega}}^T k(\mathbf{D},\mathbf{x}) + \widehat{\boldsymbol{\omega}}^T k(\mathbf{D},\mathbf{D})\widehat{\boldsymbol{\omega}}\right)^{1/2}. \end{aligned} \tag{15}$$

When the training dictionary is changing, we can obtain the corresponding residual. Therefore, for the STD, the mapped data according to (12) are

$$\Phi(\mathbf{x}) \approx \mathbf{A}_\Phi^b\boldsymbol{\alpha}_\Phi^b + \mathbf{A}_\Phi^t\boldsymbol{\alpha}_\Phi^t. \tag{16}$$

The residual between the test sample and the reconstruction in the feature space is then computed according to (15) by

$$\begin{aligned} r_{k-b}(\mathbf{x}) &= \left\|\Phi(\mathbf{x}) - \mathbf{A}_\Phi^b\widehat{\boldsymbol{\alpha}}_\Phi^b\right\| \\ &= \left(k(\mathbf{x},\mathbf{x}) - 2\widehat{\boldsymbol{\alpha}}_\Phi^{bT}k(\mathbf{A}^b,\mathbf{x}) + \widehat{\boldsymbol{\alpha}}_\Phi^{bT}k(\mathbf{A}^b,\mathbf{A}^b)\widehat{\boldsymbol{\alpha}}_\Phi^b\right)^{1/2} \\ r_{k-t}(\mathbf{x}) &= \left\|\Phi(\mathbf{x}) - \mathbf{A}_\Phi^t\widehat{\boldsymbol{\alpha}}_\Phi^t\right\| \\ &= \left(k(\mathbf{x},\mathbf{x}) - 2\widehat{\boldsymbol{\alpha}}_\Phi^{tT}k(\mathbf{A}^t,\mathbf{x}) + \widehat{\boldsymbol{\alpha}}_\Phi^{tT}k(\mathbf{A}^t,\mathbf{A}^t)\widehat{\boldsymbol{\alpha}}_\Phi^t\right)^{1/2}. \end{aligned} \tag{17}$$

The detection decision is then made by

$$D_{\mathrm{KSTD}}(\mathbf{x}) = r_{k-b}(\mathbf{x}) - r_{k-t}(\mathbf{x}). \tag{18}$$

For SRBBHD, the mapped data are

$$\begin{aligned} &H_0 : \Phi(\mathbf{x}) \approx \mathbf{A}_\Phi^b\boldsymbol{\gamma}_\Phi, \ \text{target absent} \\ &H_1 : \Phi(\mathbf{x}) \approx \mathbf{A}_\Phi^b\boldsymbol{\beta}_\Phi^b + \mathbf{A}_\Phi^t\boldsymbol{\beta}_\Phi^t = \mathbf{A}_\Phi\boldsymbol{\beta}_\Phi, \ \text{target present} \end{aligned} \tag{19}$$

where $\mathbf{A}_\Phi^b$ and $\mathbf{A}_\Phi^t$ are the background and target subdictionaries in the feature space, respectively, corresponding to $\mathbf{A}^b$ and $\mathbf{A}^t$. $\mathbf{A}_\Phi$ is the union dictionary. $\boldsymbol{\gamma}_\Phi$ and $\boldsymbol{\beta}_\Phi$ are vectors whose entries, respectively, correspond to the weighting of the samples in $\mathbf{A}_\Phi^b$ and $\mathbf{A}_\Phi$, and can be solved by KOMP.

The residual between the test sample and the reconstruction in terms of the background or target and background dictionary under different hypotheses in the feature space is then computed by

$$\begin{aligned} r_{k-0}(\mathbf{x}) &= \left\|\Phi(\mathbf{x}) - \mathbf{A}_\Phi^b\widehat{\boldsymbol{\gamma}}_\Phi\right\| \\ &= \left(k(\mathbf{x},\mathbf{x}) - 2\widehat{\boldsymbol{\gamma}}_\Phi^T k\big(\mathbf{A}^b,\mathbf{x}\big) + \widehat{\boldsymbol{\gamma}}_\Phi^T k\big(\mathbf{A}^b,\mathbf{A}^b\big)\widehat{\boldsymbol{\gamma}}_\Phi\right)^{1/2} \\ r_{k-1}(\mathbf{x}) &= \left\|\Phi(\mathbf{x}) - \mathbf{A}_\Phi\widehat{\boldsymbol{\gamma}}_\Phi\right\| \\ &= \left(k(\mathbf{x},\mathbf{x}) - 2\widehat{\boldsymbol{\beta}}_\Phi^T k(\mathbf{A},\mathbf{x}) + \widehat{\beta}_\Phi^T k(\mathbf{A},\mathbf{A})\widehat{\boldsymbol{\beta}}_\Phi\right)^{1/2} \end{aligned} \tag{20}$$

where $\widehat{\boldsymbol{\gamma}}_\Phi$ and $\widehat{\boldsymbol{\beta}}_\Phi$ are the estimations for $\boldsymbol{\gamma}_\Phi$ and $\boldsymbol{\beta}_\Phi$, respectively. The detection decision is then made by

$$D_{\mathrm{KSRBBHD}}(\mathbf{x}) = r_{k-0}(\mathbf{x}) - r_{k-1}(\mathbf{x}). \tag{21}$$

C. Final Scheme for KSRBBHD

According to the aforementioned descriptions, the implementation details of the proposed KSRBBHD algorithm for HSI are shown in Table I.

IV. Hyperspectral Data Experiments

In this section, we investigate the effectiveness of the proposed SRBBHD and KSRBBHD algorithm with two hyperspectral images.

TABLE I
PROPOSED KSRBBHD ALGORITHM FOR HSI

1.	**Input:** HSI and parameters: 1) the sizes of dual window; 2) the sparsity level; and 3) the kernel parameter
2.	**For** each test pixel $\mathbf{x}$ in the hyperspectral image scene:
	1) Construct the training samples and dictionary $\mathbf{A}^b$
	2) Construct the target pixel set $\{\mathbf{a}_i^t\}_{i=1,2,\cdots N_t}$ and then construct dictionary $\mathbf{A}$ via the target and background pixel set
	3) Recover the sparse vectors $\widehat{\boldsymbol{\gamma}}_\Phi$ and $\widehat{\boldsymbol{\beta}}_\Phi$ via KOMP
	4) Calculate the residuals $r_{k-0}(\mathbf{x})$ and $r_{k-1}(\mathbf{x})$ via (20)
	5) Calculate the discrepancy between the two residuals
	6) Turn to the next pixel
	End for
3.	**Output:** A 2-D matrix which records the detection values of each pixel

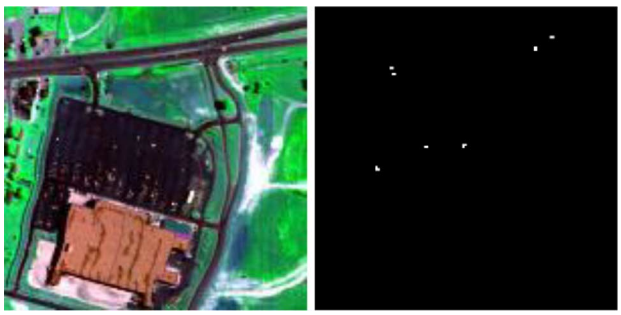

Fig. 1. HYDICE image scene and the ground-truth information.

A. Hyperspectral Datasets

The first dataset was collected by the Hyperspectral Digital Image Collection Experiment (HYDICE) sensor [30]. The dataset size is 150×150 pixels, with 210 spectral bands in the visible-NIR range. The spatial resolution is 2 m, and the spectral resolution is 10 nm. After removing the water absorption, low-SNR, and bad bands (1–4, 76, 87, 101–111, 136–153, and 198–210), 162 bands of the data were retained. This dataset is an urban scene in which there are 18 pixels as targets to be detected. A false-color map of the image data and the ground-truth information are displayed in Fig. 1.

The second dataset was collected by the Airborne Visible/Infrared Imaging Spectrometer (AVIRIS) from San Diego, CA, USA [16], [31]. The spatial resolution is 3.5 m per pixel. The image has 224 spectral channels in wavelengths ranging from 370 to 2510 nm. After removing the bands that correspond to the water absorption regions, low-SNR, and bad bands (1–6, 33–35, 97, 107–113, 153–166, and 221–224), 189 available bands of the data were retained in the experiments. From this hyperspectral dataset, a region with the size of 200×240 pixels was selected to test the detection performance. There are six planes, which include 90 pixels as targets to be detected in the scene. Fig. 2 shows the map of the AVIRIS dataset which was adopted for the real-world target detection experiment.

B. Experimental Settings

For the HYDICE dataset, the spectral signatures of the target $\{\mathbf{a}_i^t\}_{i=1,2,\ldots,N_t}$ were collected from $N_t = 3$ pixels from two targets in the right-upper corner. The sizes of the OWR and IWR were set as 17×17 and 5×5, respectively, and there were $N_b = 264$ background training samples $\{\mathbf{a}_i^b\}_{i=1,2,\ldots,N_b}$.

Fig. 2. AVIRIS image scene and the ground-truth information.

For the AVIRIS dataset, we selected one pixel from each plane as the target atoms, and $N_t = 6$. The sizes of the OWR and IWR were set as 17×17 and 7×7, respectively, and $N_b = 240$.

KSRBBHD was compared with the aforementioned algorithms: 1) SMF; 2) MSD; 3) STD; 4) SRBBHD; 5) KSMF; 6) KMSD; and 7) KSTD. For all the detectors, we used the same given target spectrum as the input *a priori* target spectrum. In the case of SMF and KSMF, the target signature was the mean of the target atoms. We adopted the pixels falling in the OWR to estimate the background covariance matrix in SMF and MSD, to construct the background atoms in STD and SRBBHD, and to estimate the kernel matrix in KMSD and KSMF. In the case of MSD, the eigenvectors corresponding to the significant eigenvalues of the covariance matrices were used to generate the basis for the subspaces. The KOMP algorithm was used to solve the sparse recovery problem in the feature space, and the OMP algorithm was used to solve the linear sparse recovery problems.

The detection performance was evaluated by both receiver operating characteristic (ROC) curves and separability maps between target and background. ROC curves have been widely used as a performance evaluation tool in target detection applications [5]. They employ a detection probability P_d and a false alarm rate P_f to provide an unbiased quantitative and threshold-free performance comparison [5]. P_d and P_f are defined as

$$P_d = \frac{N_{detected}}{N_t} \quad \text{and} \quad P_f = \frac{N_{mis}}{N_{all}} \tag{22}$$

where $N_{detected}$ represents the number of detected target pixels at a certain threshold, N_t represents the number of target pixels in the image, N_{mis} represents the number of background pixels mistaken as targets, and N_{all} represents all the pixels in the image, excluding the marginal pixels at the edge of the image which were not processed during the detection, due to the dual window. Therefore, the algorithm with the highest detection rate under the same level of false alarm rate performs better. However, when the ROC curves were difficult to judge, as they performed almost the same, we calculated the area under the ROC curves (encircled by the ROC curve and the false alarm rate axis, labeled as AUC), with the one with the largest area then being chosen as the best parameter setting [32], [33].

A separability diagram between target and background can intuitively reflect how the targets are separated from the background by the detector [5]. Usually, it is assumed that a good detector can suppress the background while distinguishing the targets. Thus, a better detector can highlight the targets and suppress the background results to a smaller value and stable range, which makes the targets more prominent in the detection results. Since the detection results range of the methods can be very wide, from the point of view of convenience and impartiality, the detection results range of all the methods were normalized to the range of 0–1. The normalization method can be expressed as follows:

$$D_{\mathrm{Nor}}(\mathbf{x}) = \frac{D(\mathbf{x}) - \min(D(\mathbf{x}))}{\max(D(\mathbf{x})) - \min(D(\mathbf{x}))} \tag{23}$$

where $D(\mathbf{x})$ is the detection result of an input vector $\mathbf{x}$ for a certain detector, $\min(D(\mathbf{x}))$ and $\max(D(\mathbf{x}))$ are the minimum and maximum values of all the detection results for a certain detector, and $D_{\mathrm{Nor}}(\mathbf{x})$ is the normalized detection result.

C. Experimental Results and Analysis

1) Parameter Analysis: This section examines the effect of the parameters on the detection performance of the proposed KSRBBHD algorithm with two HSI images. There are two critical parameters in the proposed KSRBBHD algorithm, which are the kernel parameter σ of the Gaussian kernel, and the sparsity level K_0. We fixed the other parameters as the corresponding values introduced above in Section IV-B. Since there is no specific method of choosing the optimal values of the parameters σ and K_0, the parameters were tuned manually and experientially. The rough range of σ was set as [0.01, 0.1, 1, 10], which are four different magnitudes of 10. The sparsity level K_0 is an important parameter in the four sparsity-based detectors. The rough range of K_0 was set as [2], 4, 6, 8, 10, 15, 18, 20, [30], which is roughly around the number of endmembers of the HSI data.

The experimental results at the sampling ranges were determined through AUC values, as shown in Fig. 3. The results show that the sparsity level plays a secondary role in the detection performance of KSRBBHD when the value of the kernel parameter σ is small. In detail, in the HYDICE dataset, for a small σ, especially for 0.01, the detection performance changes little with the sparsity level. The case for the AVIRIS dataset remains the same, except at a too large value of sparsity level, such as 30. Furthermore, the results show that the detection performance increases with the value of σ until the parameter reaches a certain level, such as 1, then the performance decreases for both datasets. Therefore, from the point of view of comparability, the kernel parameter σ was set as 1 for all the kernel-based detectors in the experiments.

When the value of σ was set as 1, the detection performance of the four sparsity-based detectors at different values of K_0 are shown in Fig. 4. For the HYDICE dataset, in general, the results show that the detection performance of the four detectors increases with the value of K_0, until the parameter reaches a certain level, especially for STD and SRBBHD, and then the performance decreases, especially for KSTD and KSRBBHD. The parameter K_0 was set as 10, 15, 4, and 2 to ensure the best performance of STD, SRBBHD, KSTD, and KSRBBHD, respectively. For the AVIRIS dataset, the case remains the same for STD and KSRBBHD. In addition, for SRBBHD and KSTD, the detection performance of SRBBHD and KSTD reaches a good result at a small value of K_0, and then the performance reduces when the value of K_0 increases. This may be related to the training samples in the dictionary. In detail, if there are few atoms which can lead to a good recovery result, there will be a good and simple template matching result for a small value of K_0, leading to a better detection performance. The parameter K_0 was set as 4, 2, 4, and 8 to ensure the best performance of STD, SRBBHD, KSTD, and KSRBBHD, respectively. The reason for this generally regular pattern may be that, for a very small K_0, the sparsity-based techniques reduce to a simple template matching and lead to underfitting, which usually leads to a weakening of the final target detection performance. If K_0 is too large, the solution becomes dense. Furthermore, if the characteristic between the added background and target atoms is inferior, its discriminative power degrades.

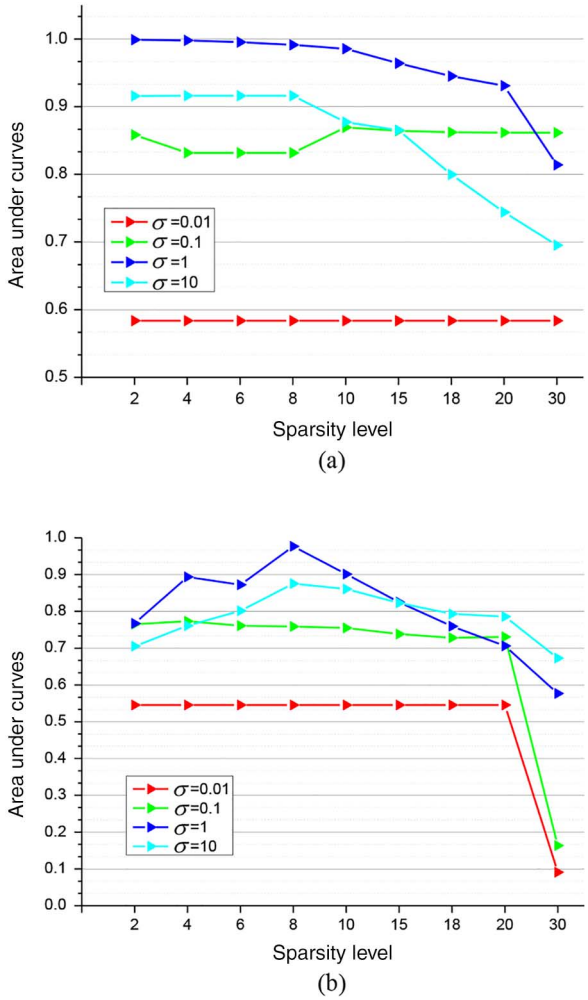

Fig. 3. AUC values of KSRBBHD at different values of σ and K_0 for two datasets. (a) HYDICE. (b) AVIRIS.

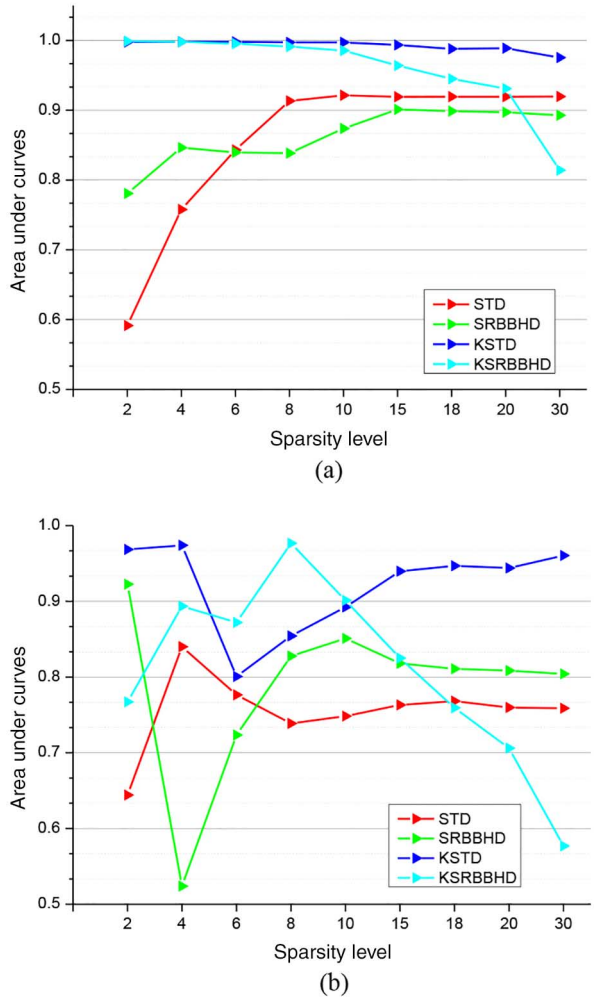

Fig. 4. AUC values of the four sparsity-based detectors at different values of K_0 when $\sigma = 1$ for two datasets. (a) HYDICE. (b) AVIRIS.

2) Detection Performance: The detection performance of KSRBBHD was evaluated and compared to the other seven detectors. The experimental results for the eight detectors at the optimal values of σ and K_0 were determined via ROC curves and AUC values, as shown in Fig. 5. The x- and y-axes, respectively, represent the detection rate and the false alarm rate. Thus, a curve near to the upper left side demonstrates a better detection performance. It can be seen from Fig. 5 that the kernelization improves the performance of the two sparsity-based detectors, STD and SRBBHD. KSRBBHD has the best detection capability, not only among the kernel-based detectors, but it also outperforms the linear detectors, as it keeps the false alarm rate at a lower level under the same detection rate. In the four linear detectors, the sparsity-based detectors STD and SRBBHD outperform the linear mixing model-based detectors SMF and MSD.

We can also see from Fig. 5(a) and (b) that STD outperforms the proposed SRBBHD with the HYDICE dataset. The reason for this may be that a good performance of SRBBHD relies on dictionaries with a good separability for the two hypotheses. However, in the reality application, the background-only

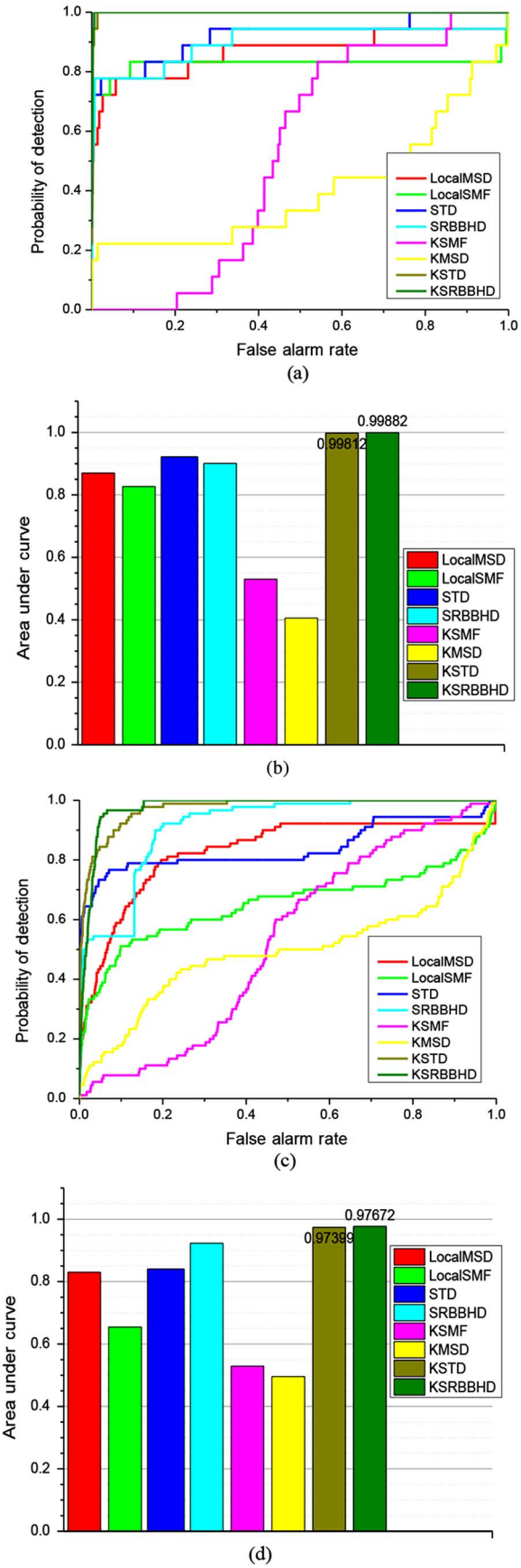

Fig. 5. ROC curves and AUC values for two datasets. (a) HYDICE, ROC. (b) HYDICE, AUC. (c) AVIRIS, ROC. (d) AVIRIS, AUC.

dictionary is usually contaminated with target samples or the background samples with weak discriminative power to the target, which will lead to a weakened separability between the two dictionaries for the two hypotheses, resulting in a severely decreased competition between the two hypotheses. In detail, the utilization of the dual window for the local background dictionary construction inevitably causes a common problem: during the sliding window process, part of the target pixels in the image may still fall into the outer window, which will result in an impure background dictionary and lead to a weakened discriminative performance for SRBBHD. Further, the spectra of certain background materials may be similar to the target spectra. When such background pixels with weak discriminative power to the target are employed for background dictionary, the competition between the two hypotheses will also be weakened. However, with the kernelization, we can see from the experimental results that the performance of KSRBBHD is improved compared to SRBBHD, and it outperforms KSTD with both datasets. This point demonstrates that the kernelization of SRBBHD can improve the separability between target and background, which is the reason why we proposed KSRBBHD.

3) Separability Analysis: To further investigate the detection performance of KSRBBHD, the separability between target and background was evaluated and compared to the other detectors via a separability map, as shown in Fig. 6. After statistical calculation of the detection values of each pixel, boxes are drawn to enclose the main parts of the pixels, excluding the biggest 10% and the smallest 10%. There are target and background columns for each detector. The lines at the top and bottom of each column are the extreme values, which are the normalized detection values by (23). The green boxes illustrate the distribution of the target pixels' values, and the line in the middle of the box is the mean of the pixels. In a similar way, the orange boxes enclose the middle 80% of the main pixels of the background pixels. The position of the boxes reflects the tendency and compactness of the distribution of the pixels. In other words, the position reflects the separability of the target and background.

For the HYDICE dataset, the detection becomes complicated as the target ranges and background ranges overlap in all the detectors. In addition, the area of the target box is completely overlapped with the background box for MSD, SMF, SRBBHD, KSMF, and KMSD. For STD, the target and background boxes have some overlapping areas, while in KSTD and KSRBBHD, the two boxes present an obvious gap. Furthermore, KSRBBHD outperforms KSTD, since KSRBBHD can effectively suppress the background information in this dataset, especially the middle 80% of the main background pixels.

For the AVIRIS dataset, the target ranges and background ranges overlap in all the detectors. In addition, the area of the target box is completely overlapped with the background box for MSD, SMF, KSMF, and KMSD. In STD, the target and background boxes have some overlapping areas, while in KSTD and KSRBBHD, the two boxes hardly present any overlapping areas. Compared to KSTD, KSRBBHD can effectively suppress the background information in this dataset, especially the middle 80% of the main background pixels. Furthermore, the target range of KSRBBHD is smaller than KSTD, which means that the power of the targets can be concentrated by KSRBBHD.

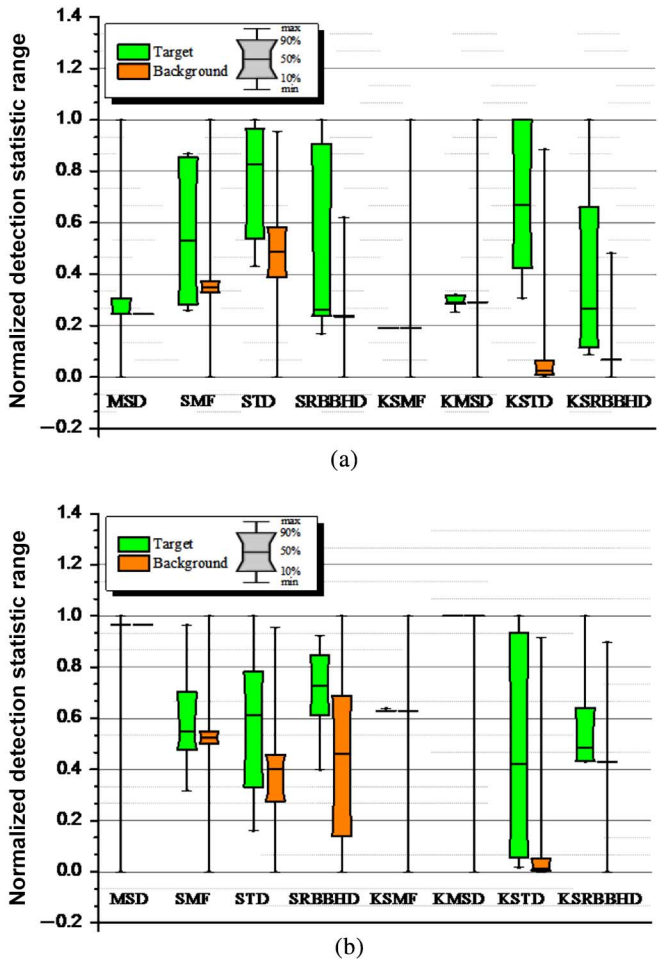

Fig. 6. Separability maps for two datasets. (a) HYDICE. (b) AVIRIS.

V. Conclusion

This paper has proposed a sparse representation-based binary hypothesis (SRBBH) model with more reasonable dictionaries for hyperspectral target detection, which models the test pixel with the background training samples under the null hypothesis, and with both the target and background training samples under the alternative hypothesis. The proposed SRBBHD algorithm utilizes the prior information of the class label for the training samples, not only in the preprocessing step in recovering the sparse vector, but also in the postprocessing when calculating the residuals. Furthermore, taking both the spectral signal representation and the complex data structure in a real HSI scene into consideration, a kernel version of SRBBHD (KSRBBHD) is proposed to solve the complicated detection problem of real hyperspectral images.

The proposed KSRBBHD was tested on two real HSI datasets, and the extensive experimental results confirm the effectiveness of the proposed SRBBHD and KSRBBHD. From

the detection results, it can be concluded that: 1) the sparsity-based detectors outperform the LMM-based detectors, and the performance of STD and SRBBHD is better than SMF and MSD; 2) the kernelization can improve the performance of the sparsity-based detectors, and KSRBBHD presents a good detection performance in complicated HSI datasets; and 3) KSRBBHD can effectively suppress the background information, especially the middle part of the main background pixels.

However, the kernel-based methods also have deficiencies, such as the selection of optimal parameters, which will be the focus of our future work. We will also investigate the effect of an impure background dictionary on the performance of SRBBHD and KSRBBHD.

ACKNOWLEDGMENT

The authors would like to thank the handling editor and anonymous reviewers for their careful reading and helpful remarks.

REFERENCES

[1] C.-I. Chang, "Target signature-constrained mixed pixel classification for hyperspectral imagery," *IEEE Trans. Geosci. Remote Sens.*, vol. 40, no. 5, pp. 1065–1081, Aug. 2002.

[2] H. Kwon and N. M. Nasrabadi, "Kernel matched subspace detectors for hyperspectral target detection," *IEEE Trans. Pattern Anal. Mach. Intell.*, vol. 28, no. 2, pp. 178–194, Feb. 2006.

[3] L. Zhang, B. Du, and Y. Zhong, "Hybrid detectors based on selective endmembers," *IEEE Trans. Geosci. Remote Sens.*, vol. 48, no. 6, pp. 2633–2646, May 2010.

[4] B. Du, L. Zhang, L. Zhang, T. Chen, and K. Wu, "A discriminative manifold learning based dimension reduction method for hyperspectral classification," *Int. J. Fuzzy Syst.*, vol. 14, no. 2, pp. 272–277, Jun. 2012.

[5] D. Manolakis and G. Shaw, "Detection algorithms for hyperspectral imaging applications," *IEEE Signal Process. Mag.*, vol. 19, no. 1, pp. 29–43, Jan. 2002.

[6] S. Matteoli, M. Diani, and G. Corsini, "A tutorial overview of anomaly detection in hyperspectral images," *IEEE Aerosp. Electron. Syst. Mag.*, vol. 25, no. 7, pp. 5–28, Jul. 2010.

[7] B. Du and L. Zhang, "Random-selection-based anomaly detector for hyperspectral imagery," *IEEE Trans. Geosci. Remote Sens.*, vol. 49, no. 5, pp. 1578–1589, Apr. 2011.

[8] J. B. Adams, M. O. Smith, and A. R. Gillespie, "Imaging spectroscopy: Interpretation based on spectral mixture analysis," in *Remote Geochemical Analysis: Elemental and Mineralogical Composition*, C. M. Pieters and P. A. J. Englert, Eds. Cambridge, U.K.: Cambridge Univ. Press, 1993, ch. 7, pp. 145–166.

[9] D. Manolakis, D. Marden, and G. A. Shaw, "Hyperspectral image processing for automatic target detection applications," *J. Lincoln Lab.*, vol. 14, no. 1, pp. 79–116, 2003.

[10] L. L. Scharf and B. Friedlander, "Matched subspace detectors," *IEEE Trans. Signal Process.*, vol. 42, no. 8, pp. 2146–2157, Aug. 1994.

[11] Q. Du and H. Ren, "Real-time constrained linear discriminant analysis to target detection and classification in hyperspectral imagery," *Pattern Recognit.*, vol. 36, no. 1, pp. 1–12, 2003.

[12] J. Wright, A. Y. Yang, A. Ganesh, S. Sastry, and Y. Ma, "Robust face recognition via sparse representation," *IEEE Trans. Pattern Anal. Mach. Intell.*, vol. 31, no. 2, pp. 210–227, Feb. 2009.

[13] Y. Chen, N. M. Nasrabadi, and T. D. Tran, "Sparse representation for target detection in hyperspectral imagery," *IEEE J. Sel. Topics Signal Process.*, vol. 5, no. 3, pp. 629–640, Jun. 2011.

[14] Y. Chen, N. M. Nasrabadi, and T. D. Tran, "Simultaneous joint sparsity model for target detection in hyperspectral imagery," *IEEE Geosci. Remote Sens. Lett.*, vol. 8, no. 4, pp. 676–680, Jul. 2011.

[15] B. Ma and Q. Du, "Hyperspectral target detection with sparseness constraint," in *Proc. IEEE Int. Conf. Geosci. Remote Sens. Symp. (IGARSS)*, Melbourne, Australia, Jul. 2013, pp. 1059–1062.

[16] T. Wang, B. Du, and L. Zhang, "A Kernel-based target-constrained interference-minimized filter for hyperspectral sub-pixel target detection," *IEEE J. Sel. Topics Appl. Earth Observ. Remote Sens.*, vol. 6, no. 2, pp. 626–637, Apr. 2013.

[17] H. Kwon and N. M. Nasrabadi, "Kernel orthogonal subspace projection for hyperspectral signal classification," *IEEE Trans. Geosci. Remote Sens.*, vol. 43, no. 12, pp. 2952–2962, Nov. 2005.

[18] X. Jiao and C.-I. Chang, "Kernel-based constrained energy minimization," in *Proc. 15th SPIE Algor. Technol. Multispectral Hyperspectral Ultraspectral Imagery*, 2008, vol. 6966, pp. 69661S1–69661S11.

[19] H. Kwon and N. M. Nasrabadi, "A comparative study of Kernel spectral matched signal detectors for hyperspectral target detection," in *Proc. 11th SPIE Algor. Technol. Multispectral Hyperspectral Ultraspectral Imagery*, 2005, vol. 5806, pp. 827–838.

[20] J. A. Tropp and S. J. Wright, "Computational methods for sparse solution of linear inverse problems," *Proc. IEEE*, vol. 98, no. 6, pp. 948–958, Jun. 2010.

[21] J. A. Tropp and A. C. Gilbert, "Signal recovery from random measurements via orthogonal matching pursuit," *IEEE Trans. Inf. Theory*, vol. 53, no. 12, pp. 4655–4666, Dec. 2007.

[22] K.-R. Müller, S. Mika, G. Rätsch, K. Tsuda, and B. Scholkopf, "An introduction to kernel-based learning algorithms," *IEEE Trans. Neural Netw.*, vol. 12, no. 2, pp. 181–201, 2001.

[23] M. Di You, *Model Selection in Kernel Methods*. Columbus, OH, USA: Ohio State Univ., 2011.

[24] A. J. Smola and B. Schölkopf, *Learning With Kernels*. Cambridge, MA, USA: MIT Press, 1998.

[25] D. You, O. C. Hamsici, and A. M. Martinez, "Kernel optimization in discriminate analysis," *IEEE Trans. Pattern Anal. Mach. Intell.*, vol. 33, no. 3, pp. 631–638, Jan. 2011.

[26] H. Kwon, S. Z. Der, and N. M. Nasrabadi, "Dual-window-based anomaly detection for hyperspectral imagery," in *Proc. SPIE*, 2003, vol. 5094, pp. 148–158.

[27] A. Banerjee, P. Burlina, and C. Diehl, "A support vector method for anomaly detection in hyperspectral imagery," *IEEE Trans. Geosci. Remote Sens.*, vol. 44, no. 8, pp. 2282–2291, Aug. 2006.

[28] Y. Chen, N. M. Nasrabadi, and T. D. Tran, "Kernel sparse representation for hyperspectral target detection," in *Proc. IEEE Int. Conf. Geosci. Remote Sens. Symp. (IGARSS)*, 2012, pp. 7484–7487.

[29] Y. Chen, N. M. Nasrabadi, and T. D. Tran, "Hyperspectral image classification via kernel sparse representation," in *Proc. 18th IEEE Int. Conf. Image Process. (ICIP)*, Sep. 2011, pp. 1233–1236.

[30] Y. Zhang, B. Du, and L. Zhang, "Regularization framework for target detection in hyperspectral imagery," *IEEE Geosci. Remote Sens. Lett.*, vol. 11, no. 1, pp. 313–317, Jan. 2014.

[31] L. Zhang, L. Zhang, D. Tao, and X. Huang, "Sparse transfer manifold embedding for hyperspectral target detection," *IEEE Trans. Geosci. Remote Sens.*, vol. 52, no. 2, pp. 1030–1043, Feb. 2014.

[32] J. Davis and M. Goadrich, "The relationship between Precision-Recall and ROC curves," in *Proc. 23rd Int. Conf. Mach. Learn.*, Pittsburgh, PA, USA, 2006, pp. 233–240.

[33] X. Sun, N. Li, and H. Zhao, "Performance evaluation for hyperspectral target detection algorithms," in *Proc. SPIE 7th Int. Symp. Instrum. Control Technol.: Sensors Instrum. Comput. Simul. Artif. Intell.*, 2008, vol. 7127, pp. 712725–712726.

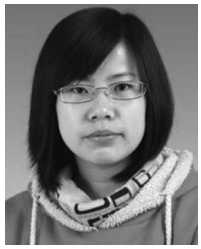

Yuxiang Zhang (S'13) received the B.S. degree in sciences and techniques of remote sensing from Wuhan University, Wuhan, China, in 2011. She is currently pursuing the Ph.D. degree in the photogrammetry and remote sensing from Wuhan University, Wuhan, China.

Her research interests include hyperspectral image processing, target detection, sparse representation, and signal processing.

Liangpei Zhang (M'06–SM'08) received the B.S. degree in physics from Hunan Normal University, Changsha, China, in 1982, the M.S. degree in optics from the Xi'an Institute of Optics and Precision Mechanics, Chinese Academy of Sciences, Xi'an, China, in 1988, and the Ph.D. degree in photogrammetry and remote sensing from Wuhan University, Wuhan, China, in 1998.

He is currently the Head of the Remote Sensing Division, State Key Laboratory of Information Engineering in Surveying, Mapping, and Remote Sensing, Wuhan University. He is also a "Chang-Jiang Scholar" Chair Professor appointed by the Ministry of Education of China. He is currently a Principal Scientist for the China State Key Basic Research Project (2011–2016) appointed by the Ministry of National Science and Technology of China to lead the remote sensing program in China. He has more than 350 research papers. He is the holder of 10 patents. His research interests include hyperspectral remote sensing, high-resolution remote sensing, image processing, and artificial intelligence.

Dr. Zhang is a Executive Member (Board of Governor) of the China National Committee of International Geosphere–Biosphere Programe, Executive Member of the China Society of Image and Graphics, etc. He regularly serves as a Cochair of the series SPIE Conferences on Multispectral Image Processing and Pattern Recognition, Conference on Asia Remote Sensing, and many other conferences. He edits several conference proceedings, issues, and Geoinformatics Symposiums. He also serves as an Associate Editor of the IEEE Transactions on Geoscience and Remote Sensing, *International Journal of Ambient Computing and Intelligence, International Journal of Image and Graphics, International Journal of Digital Multimedia Broadcasting, Journal of Geospatial Information Science*, and *Journal of Remote Sensing*.

Bo Du (M'10) received the B.S. degree in image engineering from Wuhan Univeristy, Wuhan, China, in 2005, and the Ph.D. degree in photogrammetry and remote sensing from the State Key Lab of Information Engineering in Surveying, Mapping, and Remote sensing, Wuhan University, Wuhan, China, in 2010.

He is currently an Associate Professor with the School of Computer, Wuhan University. His research interests include pattern recognition, hyperspectral image processing, and signal processing.

Shugen Wang (M'03) received the B.S. degree in aerial photogrammetry from Wuhan College of Surveying and Mapping, Wuhan, China, in 1984, the M.S. degree in photogrammetry and remote sensing from Wuhan University of Surveying and Mapping Science and Technology, Wuhan, China, in 1994, and the Ph.D. degree in photogrammetry and remote sensing from Wuhan University, Wuhan, China, in 2003.

He is currently a Professor with the School of Remote Sensing and Information Engineering, Wuhan University. His research interests include digital photogrammetry, high spatial resolution remote sensing image processing, and computer vision.